



Grain-scale modelling of swelling granular materials; application to super absorbent polymers



T. Sweijen^{a,*}, B. Chareyre^b, S.M. Hassanizadeh^a, N.K. Karadimitriou^c

^a Utrecht University, Department of Earth Sciences, Utrecht, The Netherlands

^b University Grenoble Alpes, 3SR, Grenoble, France

^c University of Manchester, School of Chemical Engineering and Analytical Science, Manchester, United Kingdom

ARTICLE INFO

Article history:

Received 12 October 2016

Received in revised form 15 March 2017

Accepted 6 June 2017

Available online 9 June 2017

Keywords:

Swelling

Super absorbent polymers

Discrete element method

Grain-scale modelling

Hydromechanical coupling

Granular materials

ABSTRACT

Swelling is an important process in many natural materials and industrial products, such as swelling clays, paper, and Super Absorbent Polymer (SAP) particles in hygienic products. SAP particles are capable to absorb large amounts of fluid. Each grain of SAP can absorb water 30 to 1000 times its initial mass, depending on the water composition.

To gain insight in the swelling behaviour of a bed of SAP particles, we have developed a grain-scale model and have tested it by comparing it to experiments. The grain-scale model is based on a combination of the Discrete Element Method (DEM) and the Pore Finite Volume (PFV) method, which we have extended to account for the swelling of individual SAP particles. Using this model, we can simulate the behaviour of individual particles inside a water-saturated bed of swelling SAP particles while taking into account the hydro-mechanical effect arising from the presence of pore water. The model input includes physical parameters such as particle stiffness and friction angle, which were found in the literature, as well as particle size distribution and diffusion coefficients, which were measured experimentally. A swelling rate equation was developed to simulate the swelling of individual particles based on water diffusion into a spherical particle. We performed experiments to measure the rise of the surface of a bed of initially dry SAP particles, which were put inside a glass beaker that contained sufficient amount of water for the SAP particles to swell and to remain saturated at all times. We used our model to simulate the swelling of that SAP particle bed as a function of time. Simulations show that the numerical model is in accordance with the experimental data. We have also verified the model with Terzaghi's analytical solution for a small swelling event. Finally, a sensitivity analysis was performed to study the effects of main grain-scale parameters on the larger-scale behaviour of a bed of particles.

© 2017 The Author(s). Published by Elsevier B.V. This is an open access article under the CC BY license (<http://creativecommons.org/licenses/by/4.0/>).

1. Introduction

Swelling of porous media occurs in many natural and industrial materials e.g. clays, foods, biological tissues, papers, and absorbent polymers in hygienic products [1–5]. Swelling is a complex process that requires knowledge of the behaviour of both fluid and solid phases and their physical interactions, as well as the chemical interactions inside and around the solid phase [6,7]. The process of swelling is defined as the expansion of a (porous) solid because of absorption of a fluid. A distinction can be made between swelling solids e.g. cartilages, hydrogels, Super Absorbent Polymers (SAP), and swelling granular media, such as

a bed of SAP particles. In this work, we focus on irregularly shaped SAP particles, whose size ranges from 45 to 850 μm and are mostly used as absorbent agent in hygienic products.

During the design of SAP, the initial chemical composition determines its stiffness, absorption rate and absorption capacity [8–10]. SAP consists of long hydrophilic polymer chains (e.g. acrylic acid) which expand and bind with water during absorption. In order to prevent these polymers from dissolving into water, other polymers are used to bind them, which are referred to as cross linkers. A larger cross-linker concentration increases the stiffness of a SAP particle, but at the same time reduces the maximum amount of water that it can absorb e.g. [10]. In hygienic products, the stiffness is essential as it increases the strength of a particle bed and thus allows the bed to have better flow properties [9]. However, there is an optimum number of cross-linkers that can be added as they decrease the absorption capacity.

* Corresponding author at: Utrecht University, Department of Earth Sciences, Environmental Hydrogeology group, Princetonplein 9, 3584CC Utrecht, The Netherlands.
E-mail address: T.Sweijen@uu.nl (T. Sweijen).

Physical properties not only depend on the polymer chemistry of SAP, but also on the production process which affects the shapes and sizes of particles. Particle size affects the swelling rate; the smaller the particle, the larger the surface area to volume ratio, and thus the higher the initial absorption rate [11]. In lab-controlled experiments, perfect spherical particles may be generated [12,13], which are useful for research purposes. However, in many production processes SAP particles are produced by grinding SAP slabs, resulting in angular particles with a wide range of sizes e.g [9,14,15]. Angular particles thus have two main features compared to spherical particles: they have a larger surface area to volume ratio and they are less likely to move to a packing [14]. Particle shapes also significantly affect the porosity and permeability [16] as well as the mechanical strength [17] of a bed of particles.

Numerous processes occur in a bed of swelling SAP particles. These include: flow of water into the particle bed, absorption of water by the particles, and rearrangement of particles due to swelling and deformation. The swelling of a bed of SAP particles is a highly coupled process involving both fluid and solid phases. This is often referred to as hydro-mechanical coupling [18]. The hydro-mechanical coupling in a particle bed is usually studied using macro-scale experiments and simulations e.g [1], where permeability and stiffness of a bed are important parameters, see for example [19]. However, grain-scale effects such as particle-particle friction [20], particle stiffness, and grain shape govern those macro-scale parameters. Experiments that aim to investigate the effect of grain-scale properties on macro-scale parameters are time consuming, difficult, and sometimes not feasible. An alternative is to develop a pore-scale or grain-scale model and use it alongside experimental investigations.

Perhaps the most suitable method for describing the motion of particles during swelling is the Discrete Element Method (DEM). This method allows simulations of the movement of individual grains in a granular porous medium [21] for example in soils [22,23], rocks [24], and industrial applications such as particle flow in silos [25]. The grains are considered as discrete elements that can undergo four relative motions at their contact points: sliding, rolling, spinning, and twisting. DEM has been mainly used for qualitative studies, but recent advancements have shown its capability for quantitative simulations within both the elastic and plastic regimes of deformation [22,26]. Various methods exist to extend DEM and include saturated and/or unsaturated flow. For example, DEM has been coupled to pore network models to simulate 2-dimensional fluid injection into granular materials under saturated conditions [27] and unsaturated conditions [28], but also to simulate 3-dimensional drying of granular materials [29], where the pore structure was assumed to be fixed while the particles in DEM could move. DEM has also been coupled to Lattice Boltzman [30] and to a finite difference scheme for fluid flow on a fixed grid [31]. In those previous works, simplifications were made to enable simulations of flow in DEM, namely: mono-dispersed packings rather than normally distributed packings, 2-dimensional rather than 3-dimensional, small deformations rather than large deformations. Recently, the pore finite volume (PFV) method was introduced by Chareyre et al. [32] and Catalano et al. [33] into DEM for simulating hydro mechanical coupling under saturated conditions. PFV is an efficient scheme for simulating 3-dimensional flow in the pore-space of packings of spheres (having a particle size distribution) accompanied by large deformations [34]. Tong et al. [35] found that the permeability values, which were predicted by the DEM-PFV model for packings of spheres, were in good agreement with experiments.

In those studies, however, absorption of water and swelling of particles were not included. Therefore, the possibility of large swelling of particles has been added to DEM in order to enable simulations of swelling and the corresponding deformation of a packing of particles. The aim is twofold i) to investigate whether DEM-PFV is capable to reproduce experiments of a bed of swelling particles, and ii) to study the effect of mechanical parameters on the swelling behaviour of a bed of SAP particles.

In this paper, we first describe the Discrete Element Method (DEM) and the Pore Finite Volume (PFV) model and how we included swelling of individual particles. Then, we discuss our experimental procedures and the model setup. Finally, we use our numerical model to simulate and reproduce experimental data. The model is then used for performing sensitivity analysis on how changes in various particle-scale properties would affect the macro-scale behaviour of a bed of particles.

2. Numerical model

In this research, we have extended the open-source software Yade-DEM to include swelling. Yade-DEM is a 3-dimensional discrete element code (DEM) [36]. DEM is a particle model that is capable of simulating deformation of granular materials by considering grain-scale interactions. In this research, DEM is employed to simulate the movement of 3-dimensional non-cohesive spheres inside a packing. To account for the presence of pore fluid in between the grains, Chareyre et al. [32] have coupled DEM with the Pore Finite Volume (PFV) method. In the following sections, we explain relevant parameters and equations of an existing DEM code, the extension we apply to include swelling particles, and the PFV method.

2.1. Discrete element method

DEM simulates the motion of individual particles inside particle packings during deformation. Each particle is defined by its properties such as radius (r_i), Young's modulus (E_i), density (ρ_i), Poisson ratio (ν_i), shear modulus (G_i), and friction coefficient (φ). At a contact between two particles the following processes can occur: normal deformation, shear, and sliding.

The contact mechanics are based on the soft sphere approach. Thus, if particles i and j are pushed towards each other, they may deform locally at their contact. This local deformation is assumed to be linearly elastic and it is measured by the normal displacement δ_{ij}^n [L], defined by:

$$\delta_{ij}^n = \begin{cases} 0 & \text{if } r_i + r_j \leq d_{ij} \\ r_i + r_j - d_{ij} & \text{if } r_i + r_j > d_{ij} \end{cases} \quad (1)$$

where d_{ij} [L] is the distance between the centres of particles i and j . An elastic force arises at the contact area of particles i and j , which acts towards reversing the overlap of particles. The elastic force is calculated using the Hertz-Mindlin theorem (see e.g [37]). In this theorem, small deformations are assumed to occur at the contact points between two particles such that $\delta_{ij}^n \ll \min(r_i, r_j)$. Based on the Hertz-Mindlin contact mechanics, the following effective parameters are defined for two particles i and j that are in contact with each other: the effective Young's modulus: $E_{ij} = \left(\frac{1-\nu_i^2}{E_i} + \frac{1-\nu_j^2}{E_j} \right)^{-1}$, the harmonic mean of particle radii: $r_{ij} = \frac{r_i r_j}{r_i + r_j}$, the average shear modulus: $G_{ij} = \frac{G_i + G_j}{2}$, and the averaged Poisson ratio: $\nu_{ij} = \frac{\nu_i + \nu_j}{2}$.

Normal displacement causes a normal force at a contact point f_{ij}^n [MLT⁻²], which is given by [37,38]:

$$f_{ij}^n = -k_{ij}^n (\delta_{ij}^n)^{3/2} \quad (2)$$

where k_{ij}^n [MT⁻² L^{-1/2}] is the contact stiffness in the normal direction and is given by:

$$k_{ij}^n = \frac{4}{3} E_{ij} \sqrt{r_{ij}} \quad (3)$$

In addition to normal displacement, shear may also occur. The elastic force in the tangential direction at a given time step, $(\mathbf{f}_{ij}^t)^{t+\Delta t}$ [MLT^{-2}], is history dependent and thus depends on its old value, such that:

$$(\mathbf{f}_{ij}^t)^{t+\Delta t} = (\mathbf{f}_{ij}^t)^t + k_{ij}^t \mathbf{d}_{ij}^t \Delta t \quad (4)$$

here \mathbf{d}_{ij}^t [LT^{-1}] is the relative tangential velocity and is defined as: $\mathbf{d}_{ij}^t = (\dot{\mathbf{x}}_i - \dot{\mathbf{x}}_j) + \boldsymbol{\omega}_i \times (\mathbf{x}_c - \mathbf{x}_i) - \boldsymbol{\omega}_j \times (\mathbf{x}_c - \mathbf{x}_j)$. It is a combination of the relative velocity of the two particles $(\dot{\mathbf{x}}_i - \dot{\mathbf{x}}_j)$ and their spinning: $\boldsymbol{\omega}_i \times (\mathbf{x}_c - \mathbf{x}_i)$ where $\boldsymbol{\omega}_i$ [degrees T^{-1}] is the angular velocity vector of particle i and \mathbf{x}_c [L] is the position vector of the contact point. The contact stiffness in tangential direction k_{ij}^t [MT^2] is given by:

$$k_{ij}^t = \frac{4\sqrt{r_{ij}} G_{ij}}{2 - \nu_{ij}} (\delta_{ij}^n)^{0.5} \quad (5)$$

Sliding at the contact can occur if the tangential force surpasses a threshold value, which is determined by a friction coefficient φ (which is the tangent of the particle-scale friction angle):

$$\|\mathbf{f}_{ij}^t\| \leq \varphi f_{ij}^n \quad (6)$$

All contact forces, gravitational forces, and forces arising from the presence of pore fluid (see Section 2.3) contribute to a resultant force vector. The resultant force vector is recast into an acceleration vector by using Newton's second law. The acceleration is integrated to find the velocity and location of each particle. The reader is referred to Šmilauer et al. [36] for more details. We use the implementation of the contact model by Modenese et al. [39].

2.2. Implementation of swelling particles in DEM

To extend DEM to include swelling of particles, we introduce the following two processes due to water absorption: 1) growth of particles and 2) the softening of particles. In the following sections, we describe how those two processes are implemented in the DEM model.

2.2.1. Modelling the swelling of a single particle

First, we define an absorption ratio Q_i^{abs} [–] for each individual particle i , which is based on the mass of absorbed water (M_i^w) and the dry mass of the particle (M_i^s):

$$Q_i^{abs} = \frac{M_i^w + M_i^s}{M_i^s} = \frac{(r_i)^3 \rho_w}{(r_i^0)^3 \rho_s} - \frac{\rho_w}{\rho_s} + 1 \quad (7)$$

in which r_i^0 is the initial particle radius, ρ_s is the density of dry SAP and ρ_w is the density of water. Note that the density of the particle itself varies from ρ_s to ρ_w with increasing values of Q_i^{abs} and that we assume that the water density inside the particle is the same as that of water outside the particle. The maximum value of Q_i^{abs} , denoted by Q^{max} , is assumed to be a known constant, following Diersch et al. [1] and Buchholz [11]. Q^{max} is usually measured experimentally and it depends on the composition of both the fluid and the solid; see e.g. [12,40]. The value of Q^{max} for SAP materials is around 30 to 40 g/g for urine (see e.g. [15,19]), about 200 g/g for tap water, and up to 1000 g/g for pure water.

The swelling of a SAP particle is driven by the difference in chemical potential between the SAP particle and the surrounding fluid [6]. We assume that the swelling rate is governed by the diffusion of water molecules into the SAP particle. Based on some simplifications, the

absorption of water at the particle scale can be approximated by the following equation, derived in Appendix A:

$$\frac{dQ_i^{abs}}{dt} = K_i \left(\frac{Q^{max} - Q_i^{abs}}{Q_i^{abs}} \right) \quad (8a)$$

$$K_i = \frac{3Dr_i}{(r_i^0)^3} \quad (8b)$$

in which D is a diffusion coefficient for water molecules in SAP [$\text{L}^2 \text{T}^{-1}$] and r_i^0 is the initial radius of particle i . For spherical particles, we can recast Eqs. (8a), (8b) into $\frac{dr_i}{dt}$ as function of r_i :

$$\frac{dr_i}{dt} = \frac{D \rho_s}{r_i \rho_w} \left(\frac{Q^{max} - Q_i^{abs}(r_i)}{Q_i^{abs}(r_i)} \right) \quad (9)$$

At the grain scale, we assume that water undergoes a phase transition across the solid – fluid interface when it gets absorbed, following Diersch et al. [1]. Therefore, the absorption of water is implemented by simply increasing the particle size, thus its radius. We implemented this in the model by defining a growth factor (f) such that the discretized form reads:

$$f = \frac{r^{t+\Delta t}}{r^t} = 1 + \frac{\Delta t}{r^t} \frac{dr}{dt} \quad (10)$$

where we assume that $\frac{dr}{dt} = \frac{r^{t+\Delta t} - r^t}{\Delta t}$, with $r_i^{t+\Delta t}$ being the radius at time $t + \Delta t$ and r_i^t being the radius at time t . Consider particles i and j that are in contact with each other. When the radii of particles i and j increase due to water absorption, the normal displacement, δ_{ij}^n , increases, see Eq. (1). Also the contact stiffness in normal direction (k_{ij}^n) and tangential direction (k_{ij}^t) would change, see Eqs. (3) and (5). In the end, the elastic contact force in normal direction f_{ij}^n and subsequently the tangential contact force f_{ij}^t would be affected during swelling of particles i and j , see Eqs. (2) and (4). Moreover, due to an increase in particle radius, the mass of a particle at time t , M_i^t increases to $M_i^{t+\Delta t}$ at time $t + \Delta t$, following:

$$M_i^{t+\Delta t} = M_i^t \cdot f^3 \quad (11)$$

Also, the rotational inertia of a particle \mathbf{I}_i [ML^2] is updated, according to:

$$\mathbf{I}_i^{t+\Delta t} = \mathbf{I}_i^t \cdot f^5 \quad (12)$$

Note that in writing Eqs. (11) and (12) the change in density of a particle is assumed to be negligible, which is a valid assumption because the density of the particle converges to that of water during early stages of water absorption. During which, the particle packing is typically very thin and thus the exact density is not required as gravity and buoyance forces are still insignificant.

2.2.2. Softening of particles

The stiffness of SAP particles depends on the absorption ratio. Water absorption causes a decrease of both Young's and shear moduli [10,11]. Following Buchholtz [11], we describe the shear modulus of a particle G_i [$\text{MT}^{-2} \text{L}^{-1}$] as a function of the absorption ratio (Q_i^{abs}) as follows:

$$G_i = \frac{\beta}{\sqrt[3]{Q_i^{abs}}} \quad (13)$$

where β [$\text{MT}^{-2} \text{L}^{-1}$] is constant for all particles and varies for varying polymer content in SAP particles. β is determined using a reference point (Q^{abs}, G). Eq. (13) only applies to SAP particles that have already absorbed some water and are in a rubbery state [11]. As the transition

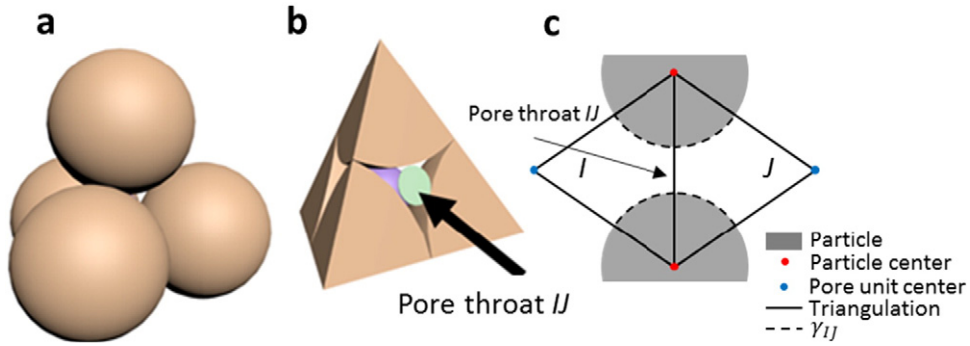


Fig. 1. Illustration of a pore unit with a) four neighbouring spheres forming a tetrahedron, b) a tetrahedron that encloses one pore unit, and c) a 2-dimensional illustration of one pore throat and its associated volumes, with γ_{ij} indicating the solid area associated with pore throat IJ . Figure adopted from [41].

from dry to rubbery state occurs at a relatively low absorption ratio, we do not consider the transition state in this work. Assuming linear deformation of the particles, the Young's modulus is related to the shear modulus, by:

$$E_i = 2G_i(1 + \nu_i) \quad (14)$$

Eqs. (13) and (14) can be implemented into Yade-DEM by simply adjusting the stiffness coefficients k_{ij}^n and k_{ij}^t which are given by Eqs. (3) and (5), respectively.

2.3. Pore-finite volume method

In order to simulate hydro-mechanical coupling, Chareyre et al. [32] have coupled the mechanical framework of DEM with a Pore-Finite Volume (PFV) method, for modelling of fluid movement through particle packings. It also allows for the computation of hydraulic properties of granular materials [35]. The PFV is briefly described here.

The first step is to apply regular triangulation to the assembly of particles, using the solid particle centres as vertices for the tetrahedra. That is, four neighbouring particles form a tetrahedron (see Fig. 1a). Each tetrahedron contains a pore space, which we refer to as a *pore unit* (see Fig. 1b). Complementary to tetrahedra are a set of Voronoi diagrams formed by the centres of pore units around a particle. Each pore unit is connected to four adjacent pore units. Consider two adjacent pore units I and J . A flat surface, or facet, separates them. This facet is the narrowest opening between the two pore units, to which we refer as throat IJ (see Fig. 1c). We assign to throat IJ a resistance to the flow of water. The resistance is calculated via a hydraulic radius, defined

as: $R_{ij}^h = \frac{\Theta_{ij}}{\gamma_{ij}}$. Here, Θ_{ij} is the void volume that is associated with pore throat IJ ; it is the void volume between three particle centres and two adjacent pore unit centres (see Fig. 1c), and γ_{ij} is the solid surface area that is present in Θ_{ij} . The hydraulic conductivity of pore throat IJ , g_{ij} [TL^5M^{-1}], is defined following Chareyre et al. [32]:

$$g_{ij} = \alpha \frac{A_{ij} R_{ij}^{h2}}{2\mu} \quad (15)$$

where A_{ij} [L^2] is the cross-sectional area of throat IJ , μ is the dynamic viscosity [$\text{MT}^{-2}\text{L}^{-1}$], and α [–] is a conductivity factor that is equal to 1 for spherical particles and smaller for other shapes. In fact, α can be used as a calibration factor to match the calculated permeability s to that of experiments. Each pore unit has a fluid pressure p [$\text{MT}^{-2}\text{L}^{-1}$] and each pore throat has a volumetric flow rate q_{ij} [L^3T^{-1}], which is proportional to the pressure difference:

$$q_{ij} = g_{ij} \frac{(p_j - p_i)}{l_{ij}} \quad (16)$$

where l_{ij} [L] is the distance in between the two pore unit centres.

2.4. Inclusion of swelling in PFV method

To implement swelling in the PFV method, we realize that the change of volume of each pore unit is a result of the relative movement of, and water absorption by, the four surrounding particles. We assign a swelling rate to each particle, which results in a rate of water absorption

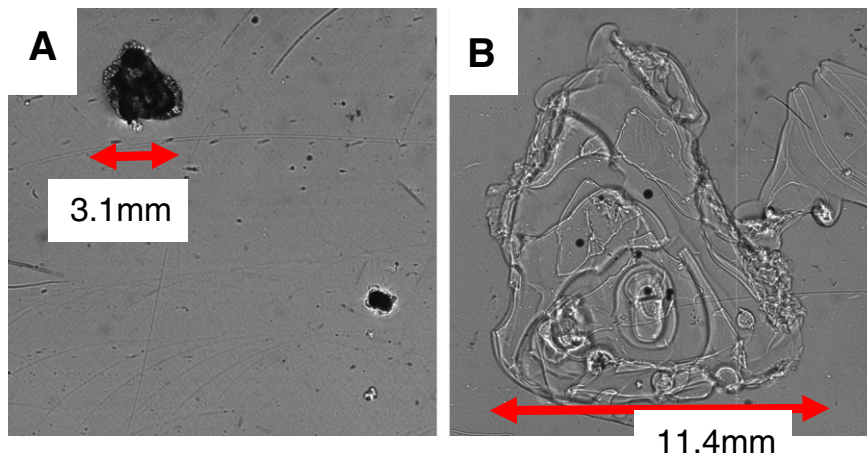


Fig. 2. Example of an SAP particle A) image of an SAP particle that is slightly swollen B) the same SAP particle in completely swollen state.

in the surrounding pore units. The change of volume of a pore unit is balanced by the net flux of water into and out of the pore unit and the rate of absorbed water:

$$\left. \frac{dV_i}{dt} \right|_{relmov} + \left. \frac{dV_i}{dt} \right|_{abs} = \sum_{j=1}^4 q_{ij} - q_i^{abs} \quad (17)$$

where $\left. \frac{dV_i}{dt} \right|_{relmov}$ is the change in pore volume of pore unit i due to relative movement of its surrounding particles (or deformation), q_i^{abs} is the absorption rate that acts in pore unit i , and $\left. \frac{dV_i}{dt} \right|_{abs}$ is the volume change of pore unit i due to swelling of the four surrounding particles. Note that the total absorption rate of one particle is the sum of $\left. \frac{dV_i}{dt} \right|_{abs}$ of all its surrounding pore units. We assume that the density of the water does not change when it gets absorbed, leading to: $\left. \frac{dV_i}{dt} \right|_{abs} = -q_i^{abs}$. Consequently, we only need to solve for pressure using the following equation:

$$\left. \frac{dV_i}{dt} \right|_{relmov} = \sum_{j=1}^4 q_{ij} \quad (18)$$

which is the same as for non-swelling media. The discretized form of Eqs. (16) in (18) yield a set of linear algebraic equations for pressure. For more information on how to solve for the fluid pressure, the reader is referred to Catalano et al. [33].

The final step is to compute the forces acting on the particle by its surrounding fluid. This includes the effects of buoyancy, viscous forces due to fluid flow, and the difference in fluid pressure surrounding a particle because of flow. For a comprehensive description of the computations of the different forces, the reader is referred to Chareyre et al. [32].

3. Experimental methods

To illustrate the application of our model, we simulated an experiment on the swelling of a bed of SAP particles inside a glass beaker, under fully saturated conditions. For this purpose, we first measured the swelling rate of individual particles and determined the particle size distribution of a batch of dry SAP particles. This information was used as input for our simulations. Finally, we measured and simulated the swelling rate of a bed of SAP particles using our model.

3.1. Experiments on individual SAP particles

3.1.1. Swelling kinetics of a single particle

To quantify the swelling rate, we used a custom-made imaging system. It consisted of a LED light source emitting at 560 nm, mounted on an objective lens F 3.2/105 mm to get a highly collimated light beam, a prism (Edmund Optics) with dimensions of 50 mm × 50 mm, a SONY

Sonnar F1.8/135 mm objective lens, and a GC-2450 Prosilica camera with a resolution of 5 Mega pixels. This optical setup was able to acquire magnified images of the swelling particle at a frame rate of up to 15 frames per second. The experimental procedure was as follows. First, a single particle was put into a Plexiglas container with dimensions 52 × 32 × 7 mm³. Sufficient water was added such that the particle was immersed at all times. At a frequency of 1 frame per second, images were taken at a resolution of 7.8 μm per pixel, for a period of 30 min. See Fig. 2 for initial and final state of a particle. The acquired images were processed with image analysis tools to determine the surface area of each particle as a function of time. Then, an equivalent circle was assigned to the surface area. This resulted in obtaining an equivalent particle radius (r_i) as a function of time (see Fig. 3A). This data was fitted using Eq. (9), where Q^{max} and D were unknown parameters. Q^{max} was determined by measuring the mass of many particles before and after swelling. The experiment was conducted as follows: approximately 2 g of dry SAP particles were put into a petri dish and subsequently hydrated. After 30 min, the mass of the swollen particles was measured. After repeating this experiment, we found $Q^{max} = 216 \text{ g/g} \pm 15\%$. D was determined as a fitting coefficient, for a large number of particles; for each particle, a value of D was fitted to experimental data with $R^2 > 0.86$. The mean value of D was computed and was found to be $4.8 \times 10^{-4} \text{ cm}^2 \cdot \text{min}^{-1}$ and D varied between $7.0 \times 10^{-4} \text{ cm}^2 \cdot \text{min}^{-1}$ and $3.0 \times 10^{-4} \text{ cm}^2 \cdot \text{min}^{-1}$.

3.1.2. Particle size distribution

Using the same imaging setup as described in Section 3.1.1, we measured the Particle Size Distribution (PSD) of dry SAP particles. A large number of particles were placed in a dry Plexiglass container such that they did not touch each other. We took images of 500 particles and calculated the equivalent radius of an equivalent circle, which is the same method to that used by Esteves [13]. Fig. 3B shows the PSD, which is relatively narrow and has a mean radius of $150 \mu\text{m} \pm 6\%$.

3.2. Experiments on a bed of swelling SAP particles

To measure the swelling kinetics of a bed of SAP particles, we placed 100 mg of dry SAP particles into a measurement cylinder with a diameter of 2.5 cm and a volume of 100 ml. This resulted in 0.02 g of SAP particles covering each cm² of the bottom of the beaker glass. Then, 60 ml of slightly dyed water was poured into the cylinder. The water was dyed to visualize the pore water, because swollen SAP particles are difficult to distinguish from water without a dye. The particles were allowed to swell for 30 min. A high-resolution camera was used to capture the swelling process. The images from the camera were carefully interpreted to determine the height of the bed of SAP particles at 30 s' intervals. The height was also measured manually for cross controlling the camera data. The height as function of time was used to test our

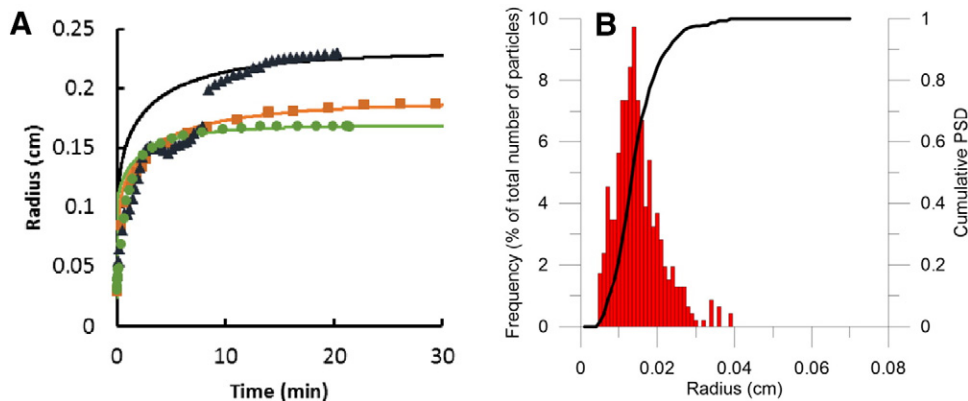


Fig. 3. A) Swelling kinetics of individual particles under saturated conditions. Each colour represents a different particle with a different initial size ($r_{i,0}$), symbols represent measurements and the dashed lines are the fittings using $D = 4.8 \times 10^{-4} \text{ cm}^2 \cdot \text{min}^{-1}$ and $Q^{max} = 216 \text{ g/g}$. B) Particle size distribution of dry SAP particles.

particle model, as we will describe in the following section. We refer to this experiment as the macro-scale swelling experiment.

4. Model setup

To simulate the swelling of a bed of SAP particles, we have chosen the values of input parameters as close as possible to those of SAP particles. In the following subsections, we explain the parameterization and model setup.

4.1. Parameterization

Table 1 shows values of physical parameters of individual SAP particles. These parameters were the density of dry SAP particles, shear modulus, Poisson ratio, and friction coefficient. The density was set to 1.6 kg/m^3 [42]. The friction coefficient φ was set to 0.096, which corresponds to the micro-scale friction angle of acrylic acid, namely 5.5° [43]. SAP particles contain complex volume cross-linked and surface cross-linked structures, and thus the friction coefficient varies for different degrees of cross-linking. Due to the complexity of measuring the friction coefficient [44], it is often determined through fitting data see e.g. [22]. But, we have chosen to set the value of the friction coefficient to that of acrylic acid. In our sensitivity analysis, we studied the effect of changing the friction coefficient. The Poisson ratio was set to 0.5, which corresponds to an incompressible solid. The relation between shear modulus and absorption ratio was parameterized by setting β to 22.1 kPa, which was based on experiments on individual SAP particles by [10]. In our sensitivity analysis, we also chose β values of 15.5 kPa and 31.1 kPa.

4.2. Modelling the experiments

A model scenario was setup to closely mimic our macro-scale swelling experiment. We considered a modelling domain of $2 \times 2 \times 20 \text{ cm}^3$ to simulate the beaker glass. A cloud of particles was generated having the particle size distribution of SAP particles, which was measured as explained in Section 3.1.2. We used 0.02 g of SAP particles for each cm^2 of bottom of the modelling domain, which was the same particle concentration that was used in our macro-scale swelling experiments. Consequently, 2720 particles were used for simulations. We performed simulations for varying number of particles in the $2 \times 2 \times 20 \text{ cm}^3$ modelling domain, to determine whether 2720 particles would be more than the minimum number of particles that are required for the results to be representative and independent of size. We found 2000 particles or more would be sufficient.

After the particle cloud was generated, we simulated the deposition of particles due to gravity. This resulted in a one-layer array of particles at the bottom of the modelling domain, as it was the case in experiments. The same particle array was used as the initial configuration for all simulations.

The boundary conditions were set to mimic a stress-free swelling experiment inside a beaker glass. The bottom and sidewalls were assumed to be rigid and subjected to no-flow boundary conditions. The upper boundary of the bed of particles, however, was allowed to move freely. The water pressure of pores along the upper boundary was set equal to zero. During the simulation, the location of the top boundary was

Table 1
parameters for SAP particles.

Parameter	Value	Sensitivity analysis	Reference
Density	1.6 kg l^{-1}	–	[42]
Poisson ratio, ν	0.5	–	
Reference shear modulus, G	7.1 kPa	5 kPa–10 kPa	@ $Q^{\text{abs}} = 30 \text{ g/g}$ [10]
β	22.1 kPa	15.5 kPa–31.1 kPa	
Friction coefficient	0.096	0.017–0.84	[43]

tracked and compared to the height of the SAP particle bed in our macro-scale swelling experiments.

The time step was allowed to vary between 10^{-7} and 10^{-5} s. It was determined as follows (see Šmilauer et al. [36] for details). For each contact point of two particles, a characteristic time step was determined based on its eigen frequency. A list of characteristic time steps was compiled and the minimum value was determined. To ensure numerical stability, the minimum value was divided by safety factor of 10 as the new time step. However, to speed up the calculations, the change of radii of particles due to water absorption was applied only once in every 500 time steps. We varied the frequency of this update and we found no effect on the swelling behaviour. Also, the pore pressure field was updated only every 500 time steps. Simulations were carried out until equilibrium was achieved in the packing, which occurred after 10 min. This was equivalent to a runtime of one-week, using a single core of a 3.2 GHz processor.

5. Verification and application of the particle model

Here, we present the results of the simulation of a bed of swelling SAP particles. First, we verify the implementation of hydro-mechanical coupling during a small swelling event. Secondly, we verify the mass conservation of water in the model during swelling of a bed of SAP particles. Then, we test the model by simulating the macro-scale swelling experiment and by comparing it with experimental data. Finally, a sensitivity analysis is done on micro-mechanical parameters.

5.1. Verification of the hydro-mechanical coupling during swelling

We have used Terzaghi's analytical solution [18] for consolidation of a porous medium to verify the pore water pressure evolution during a swelling event. Consolidation is the process where the porosity of a porous medium is decreased due to an increase in confining stress. This is, however, possible only if the pore fluid flows out of the porous medium, which is a time dependent process. Similarly, a decrease in confining stress can cause a subsequent expansion, or swelling, of the porous medium [18]. Consider a sample of SAP particles that has an absorption ratio of 10 g/g. The relaxation of excess pore water pressure after a perturbation is given by the following equations (see [33] for more detail):

$$\frac{P_w(Z, T_v)}{P_{w,0}} = \sum_{m=0}^{\infty} \frac{4}{\pi(2m+1)} \cdot \sin\left(\frac{\pi}{2}(2m+1)Z\right) \cdot e^{-\left(\frac{\pi}{2}(2m+1)\right)^2 T_v} \quad (19a)$$

$$T_v = \frac{t K_h \bar{E}}{H^2 \rho_w g} \quad (19b)$$

$$Z = \frac{z}{H} \quad (19c)$$

where P_w and P_w^0 [$\text{MT}^{-2} \text{L}^{-1}$] are the excess pore water pressure and the initial pore water pressure, respectively, H [L] is half of the thickness of the sample, Z [–] is the normalized thickness, \bar{E} [$\text{MT}^{-2} \text{L}^{-1}$] is the tangent modulus of the sample, g [LT^{-1}] is the gravitational constant and K_h [LT^{-1}] is the hydraulic conductivity of the sample.

To test our model, we have compared it to the analytical solution. We have simulated a sample of swollen SAP particles by generating 5000 particles in a modelling domain of $0.15 \times 0.15 \times 0.15 \text{ m}^3$. We used the particle size distribution that we previously measured (see Section 3.1.2), but it was scaled to a swelling ratio of 10 g/g. To confine the sample, a confining pressure of 250 Pa was applied on all six boundaries. This confining pressure corresponds to the average pressure over time for an SAP particle that is located in the centre of a bed of particles that swells from the height of one single layer to the height of a fully swollen bed of SAP particles, namely 6.76 cm (see Section 5.3.1). The particle packing was immersed in water, with the top boundary being

a water reservoir at a constant pressure of zero Pa, while the other boundaries were subjected to no-flow conditions. After the packing was generated, virtual consolidation and permeability tests were used to determine the Young's modulus (1.3 kPa) and the permeability ($7.2 \times 10^{-10} \text{ m}^2$) of the material. Next, a swelling step was applied by increasing all particle radii with a factor, $f = 1.0001$, which was a typical value during simulations of a bed of SAP particles. After the particle radii were increased, the DEM model was run until the particles were in equilibrium.

In Fig. 4, the pore pressure profiles are plotted for our simulations and those by Eqs. (19a), (19b), (19c). It is clear that the analytical solution and simulations coincide well. Therefore, we concluded that water pressure is modelled correctly during swelling.

5.2. Verification of mass balance during swelling

Here, we verify the mass balance of water in the model, by comparing the water volume in the model by the integral of the water flux across the model boundary. In addition, we use a macro-scale mass balance equation for swelling granular materials by Diersch et al. [1] to verify our results. The mass balance equation is as follows:

$$\bar{q} = 4H^0 J_v \left[\frac{\rho_s(1-\phi^0)}{\rho_w J_v} + \frac{\partial \phi}{\partial \bar{Q}} + \frac{\phi}{J_v} \frac{\partial J_v}{\partial \bar{Q}} \right] \frac{\partial \bar{Q}}{\partial t} \quad (20)$$

where $\bar{q} [\text{LT}^{-1}]$ is the water flux into the modelling domain, $\phi [-]$ is the porosity, ϕ^0 is the initial porosity, $H^0 [\text{L}]$ is the initial thickness of the bed of particles, $J_v [-]$ is the dilatation of the modelling domain such that $J_v = \frac{\bar{V}}{\bar{V}^0}$, \bar{V} and $\bar{V}^0 [\text{L}^3]$ are the volume of the modelling domain

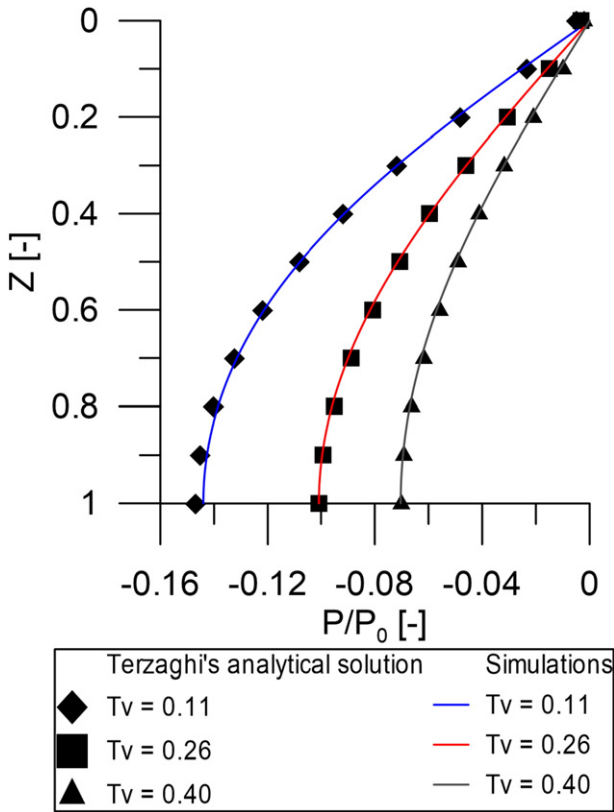


Fig. 4. Terzaghi's solution for consolidation (symbols) and one-step swelling results by Yade-DEM (solid line). Different colours represent different times. Results are for a swelling factor (f) 1.0001, absorption ratio $Q = 10 \text{ g/g}$ and a confining stress of 250 Pa.

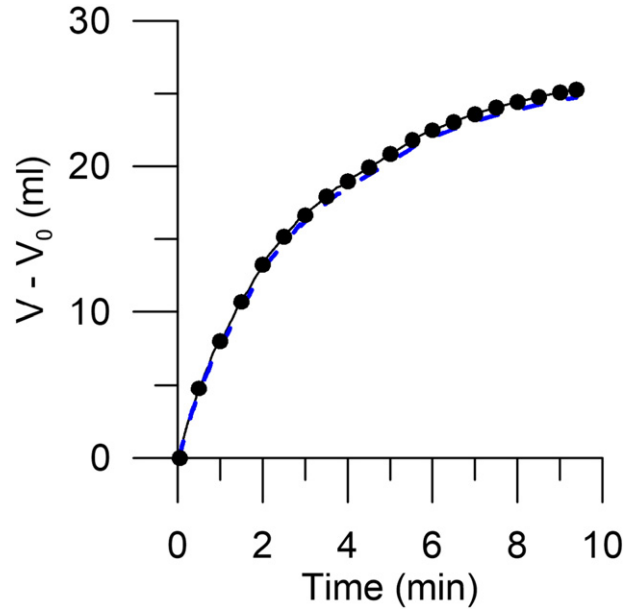


Fig. 5. Volume increase of the simulation domain due to the swelling of SAP particles. The solid line represents the volume increase as found in the model whereas the symbols shows the solution of Eq. (20), following Diersch et al. [1] and the dashed line represents the integration of the water flux as found in the PFV model.

and its initial volume, respectively. $\bar{Q} [-]$ is the macro-scale absorption ratio which is given by:

$$\bar{Q} = \frac{(\bar{V}_s - \bar{V}_s^0) \rho_w}{\bar{V}_s^0 \rho_s} \quad (21)$$

where \bar{V}_s and $\bar{V}_s^0 [\text{L}^3]$ are the total solid volume, including the absorbed water, in the modelling domain and its initial value, respectively. We have plotted the volume increase of the modelling domain with respect to its initial volume ($\bar{V} - \bar{V}^0$). We have plotted in Fig. 5 three curves of $\bar{V} - \bar{V}^0$ based on: 1) the volume of the modelling domain as found in DEM indicated by the solid line, 2) integration of the water flux through the top boundary over time as found in PFV indicated by the dotted line, and 3) integration of the flux in Eq. (20) over time indicated by the dots. In Fig. 5 results obtained with Eq. (20) corresponds very well to the volume increase of the modelling domain,

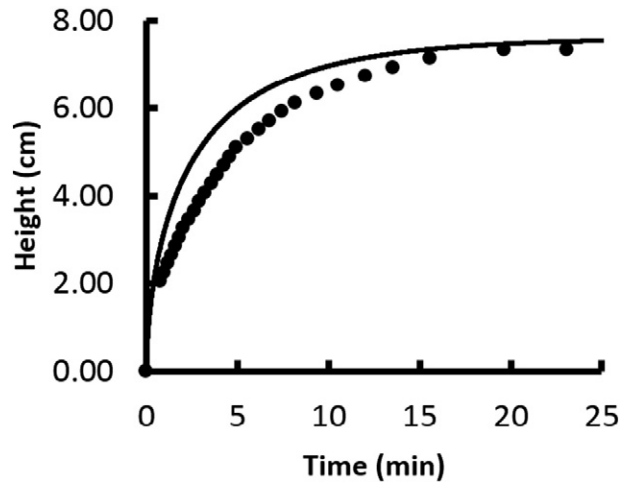


Fig. 6. Results on the evolution of the height of a bed of SAP particles during swelling. Experimental data are shown by symbols while the solid lines represent simulation results.

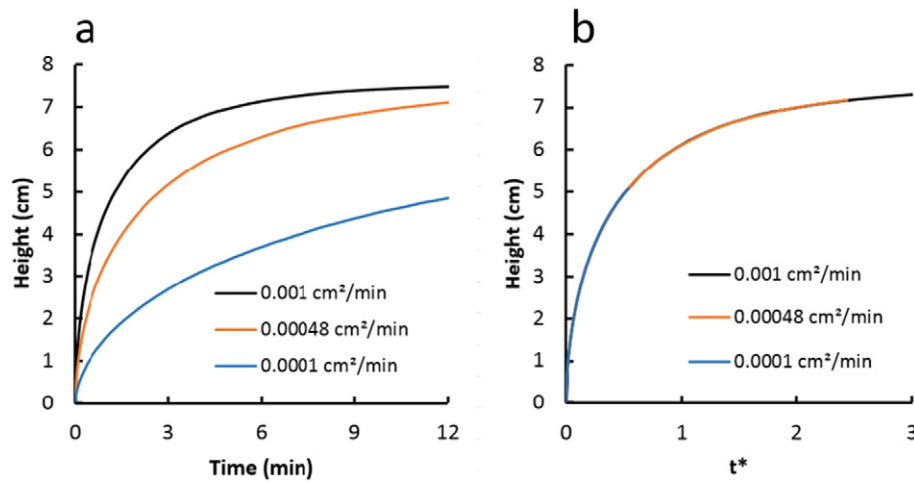


Fig. 7. The effect of the diffusion coefficient (D) on the swelling behaviour of a bed of SAP particles, a) height vs. time, and b) height vs. normalized time $t^* = \frac{tD}{H_0^2}$. H_0 is the initial height of the particle bed.

which indicates that the relation between ϕ , J_v , and \bar{Q} is modelled correctly in our model. However, the volume of water that enters via the top boundary is 2.1% lower than the actual volume increase of the modelling domain, which is probably because $\frac{dV_l}{dt}|_{relmov}$ is approximated by the change of volume of a tetrahedron rather than the void volume of a pore unit, such that the computational effort is reduced.

5.3. Simulations of a bed of SAP particles

5.3.1. Simulation of macro-scale swelling experiments

Fig. 6 shows the height of the SAP particle bed as a function of time for experiments and simulations with our model. Three main features are important in this Figure. The final height of the SAP particle bed that was simulated by our model (7.56 cm) was fairly close to the measured value (7.13 cm). The initial swelling rate in experiments and our model agree well. But, when the bed reached 2 cm, the swelling rate starts to decrease in experiments causing the simulated swelling rate to overestimate the height of the particle bed. The decrease of the swelling rate in experiments can be related to i) limited water availability inside the SAP particle bed due to clogging inside the bed, which is not present in simulations, ii) the SAP particles swell heterogeneously during swelling whereas we assume particles to remain spherical, or iii) the local confining pressure acting on the SAP particles reduces the swelling rate. In this research, however, it

is not possible to identify which process is causing the deviation in swelling rate.

5.3.2. Effect of the diffusion coefficient

The diffusion coefficient, D , may vary for varying SAP types, to study its effect on the swelling behaviour of a bed of particles, we have changed D to 1.0×10^{-4} and $1.0 \times 10^{-3} \text{ m}^2 \text{ s}^{-1}$. Results are shown in Fig. 7. It is clear from Fig. 7a that reducing D slows down the swelling of the bed of particles. To study whether the arrangement of particles was affected by a change in diffusion coefficient, other than the change in swelling kinetics, we plotted in Fig. 7b the height vs. normalized time (t^*) as: $t^* = \frac{tD}{H_0^2}$, where H_0 is the initial thickness of the particle bed. The three simulations with varying diffusion coefficient show identical evolution of height with t^* . This indicates that the particle rearrangement during swelling is not affected by changing the diffusion coefficient, and the time scales linearly with the inverse of D .

5.3.3. Effect of mechanical parameters

Here, we discuss the effect of the friction coefficient (φ) and the reference shear modulus (β) on the swelling behaviour of a bed of swelling SAP particles. The friction coefficient is a lumped parameter, which includes the friction intrinsic to the particle material and the surface roughness [44]. Both may vary for different batches of SAP particles

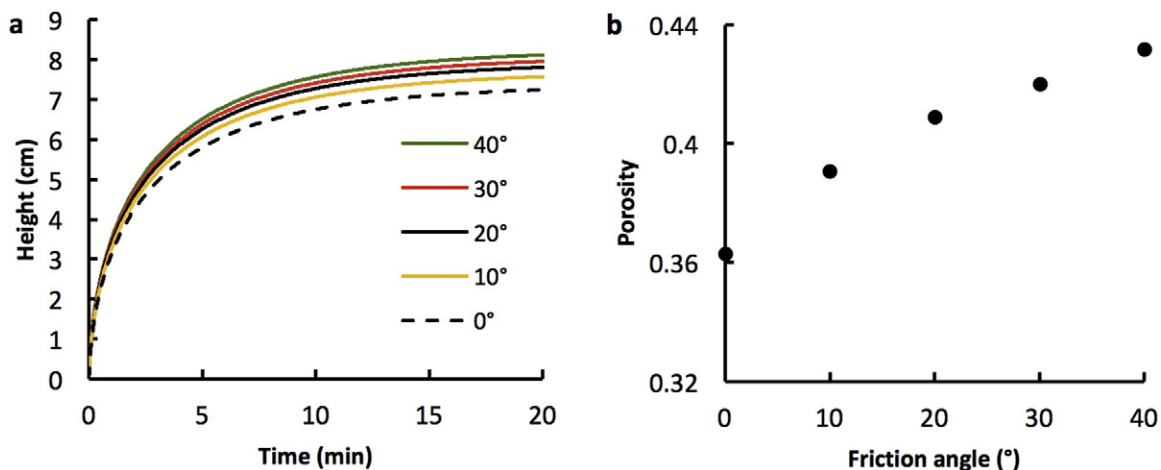


Fig. 8. Swelling of a bed of particles for different particle friction coefficients, from 0.017 to 0.84. a) height vs time b) the porosity after swelling vs the friction coefficient.

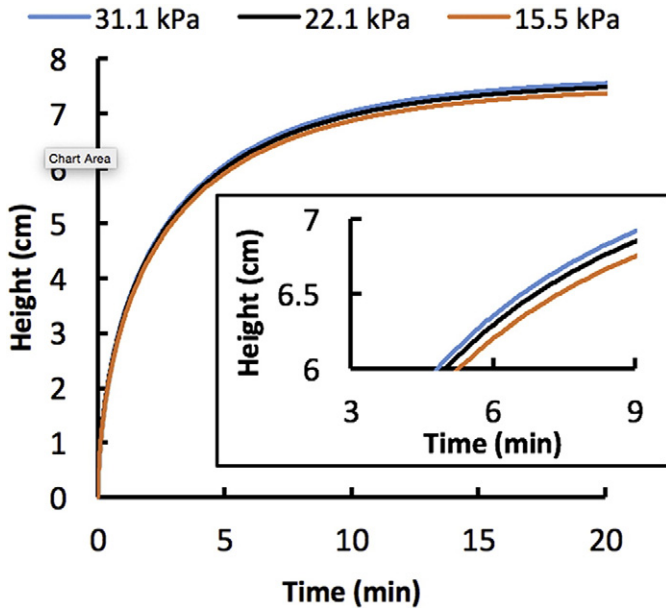


Fig. 9. The effect of reference shear modulus (G_r ; values shown in kPa) in terms of β on the swelling of a bed of particles in terms of height vs time. The insert shows the enlargement of change of height at later times.

either due to their chemical composition or due to the manufacturing process. They may also vary because of surface treatments cf. [20]. We performed a series of simulations with friction coefficients ranging from 0.017 to 0.84, corresponding to micro-scale friction angles 1° to 40° . The simulation results showed that a larger friction coefficient yields a larger height of the particle bed after swelling, as seen in Fig. 8a. In other words, after swelling with a larger friction coefficient, a larger porosity is achieved, which is evident from Fig. 8b. A larger porosity is a result of particles that cannot move and rearrange themselves easily inside a particle bed at a larger friction coefficient, in contrast to a smaller friction coefficient.

The stiffness of SAP particles, parameterized by β , may vary with their polymer chemistry [9,10]. An increase in particle stiffness of SAP particles, due to a change in their chemistry, decreases Q^{max} and may also alter the swelling behaviour of a bed of SAP particles. Here, we assume that Q^{max} remains constant but β changes. Results in Fig. 9 show that a lower β value results in more compaction of the bed under its own weight, and thus a lower height after swelling. However, the effect of β was relatively small, as the final height varies between 7.45 cm for $\beta = 15.5$ kPa to 7.64 cm for $\beta = 31.1$ kPa, compared to 7.56 cm as found for the reference case; $\beta = 22.1$ kPa.

5.3.4. Flow of water during swelling

A major issue with swelling granular materials is that blockage of pores may slow down the swelling rate of a bed of particles. In principle, there are two competing processes, namely: swelling of particles and dissipation of excess water pressure that arises due to the changes in pore spaces. In Fig. 10a, we show typical profiles of water pressure inside a bed of swelling particles at different times. In that Figure, the height is normalized with respect to the thickness of particle bed at any given time. As water gets absorbed by particles, the pressure is negative in the particle bed with the lowest value being at the bottom. This pressure gradient also corresponds to the fact that water enters the bed of particles from above and moves down the particle bed to replenish water absorbed by particles. At the end of the absorption process, water pressure distribution becomes hydrostatic. In fact, at time $t = 0$, the water pressure distribution is hydrostatic. But negative values rapidly develop as water gets absorbed. This is shown in Fig. 10b, where the water pressure averaged over the whole particle bed is plotted as function of time. A minimum value is reached within a short time (around $t = 0.4$ min for $\alpha = 1$) and then it increases slowly. Another simulation was conducted for a particle bed having a lower permeability value, using $\alpha = 0.01$. We found that both curves for height evolving over time for $\alpha = 0.01$ and $\alpha = 1$ were similar. But, simulations with $\alpha = 0.01$ did show lower values of pressure because the lower permeability (see Fig. 10b).

6. Conclusion

In this research, a particle model has been developed to simulate the swelling of granular materials. For this purpose, an existing Discrete Element Method (DEM), coupled with a Pore Finite Volume (PFV) method, was extended to include the swelling of individual particles. The model was physically based and its input parameters were derived from literature and in-house experiments. To describe the swelling rate of individual particles, an analytical equation was derived that describes the swelling rate driven by diffusion of water into SAP particles. We have performed experiments and simulations of a bed of swelling SAP particles inside a glass beaker. We find that our model results agree relatively well with experimental data, except for the swelling rate after 2 min, which was slightly faster in simulations. Sensitivity analyses were done on the friction coefficient, shear modulus, and diffusion coefficient. Model results indicate that decreasing the friction coefficient or particle stiffness lowers the porosity, and that changing the diffusion coefficient only affects the time it takes to obtain equilibrium but not the particle rearrangement. Moreover, the model indicates that during swelling, fluid has to be distributed through the particle bed. This is associated with an increase of water suction inside the particle bed. The magnitude of the suction pressure is related to the permeability of the

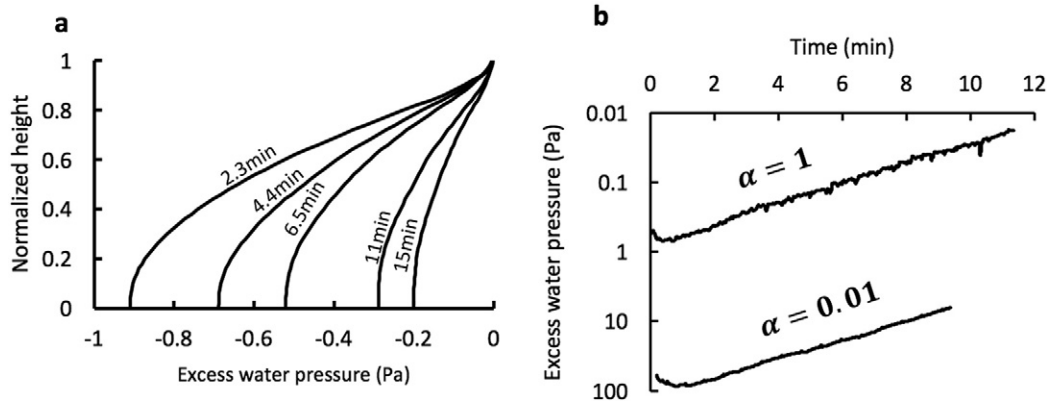


Fig. 10. a) Normalized depth vs. water pressure profiles at different times for $\alpha = 1$. b) The evolution of excess water pressure that is averaged over the whole particle bed for $\alpha = 1$ and $\alpha = 0.01$.

sample. The numerical model is a useful model to study the effect of various parameters on the complex behaviour of swelling SAP particles.

Nomenclature

Subscripts

I	Pore unit I
J	Pore unit J
IJ	Pore throat IJ
i	Particle i
j	Particle j
ij	Contact between particle i and j
c	Contact point
s	Solid
w	Water

Superscript

0	Initial value
t	Time t
$t + \Delta t$	Time $t + \Delta t$
n	Normal direction
t	Tangential direction

Symbols

α	Constant to vary the pore throat conductivity
β	Constant that controls the particle stiffness [$\text{MT}^{-2} \text{L}^{-1}$]
$\bar{\beta}$	Constant that controls the stiffness of the particle packing [$\text{MT}^{-2} \text{L}^{-1}$]
γ	Solid surface area [L^2]
δ_{ij}^0	Overlap between particle i and j [L]
Θ	Void volume [L^3]
K	Kinetic rate constant for swelling of particles [T^{-1}]
μ	Viscosity [$\text{MT}^{-1} \text{L}^{-1}$]
ν	Poisson ratio [–]
ρ	Density [ML^{-3}]
φ	Friction coefficient [–]
ϕ	Porosity [–]
ω	Angular velocity vector [degrees T^{-1}]
A	Surface area [L^2]
c	Concentration [ML^{-3}]
D	Diffusion coefficient [$\text{L}^2 \text{T}^{-1}$]
d	Distance [L]
\mathbf{d}^t	Tangential displacement vector [LT^{-1}]
\bar{E}	Youngs modulus of the bed of particles [$\text{MT}^{-2} \text{L}^{-1}$]
E	Youngs modulus of the particles [$\text{MT}^{-2} \text{L}^{-1}$]
f	Contact force [MLT^{-2}]
f	Growth factor [–]
g	Gravitational constant [LT^{-2}]
G	Shear modulus of a particle [$\text{MT}^{-2} \text{L}^{-1}$]
H	Thickness of a sample [L]
I	Inertia [ML^2]
J_v	Dilation of the modelling domain [–]
k	Conductivity [$\text{TL}^5 \text{M}^{-1}$]
K_h	Macro-scale hydraulic conductivity [LT^{-1}]
k	Contact stiffness [MT^2]
l_{ij}	Distance between two pore units [L]
M	Mass [M]
P_w	Average pore water pressure [$\text{MT}^{-2} \text{L}^{-1}$]
p	Pore water pressure [$\text{MT}^{-2} \text{L}^{-1}$]
\bar{q}	Water Darcy flux over the model boundaries [LT^{-1}]
q	Volumetric flux [$\text{L}^3 \text{T}^{-1}$]
q^{abs}	Volumetric absorption flux [$\text{L}^3 \text{T}^{-1}$]
\bar{Q}	Macro-scale absorption ratio [–]

Q^{max}	Maximum value of Q^{abs} [–]
Q^{abs}	Absorption ratio [–]
r	Particle radius [L]
\bar{r}	Average particle radius [L]
R^h	Hydraulic radius of a pore throat [L]
T_v	Dimensionless time [–]
V	Void volume of a pore unit [L^3]
\bar{V}	Volume of the modelling domain [L^3]
\mathbf{x}	Location vector [L]

Acknowledgement

The first author gratefully acknowledges financial support from the Technology Foundation STW, the technological branch of the Netherlands Organization of Scientific Research, NWO, and the Dutch ministry of Economic Affairs under contract no. 12538, entitled Interfacial effects in ionized media. The second author acknowledges the CRCT granted by Grenoble INP in 2012 which allowed this joint research. The third author would like to thank European Research Council for the support they have received for this research under the European Union's Seventh Framework Programme (FP/2007–2013)/ERC Grant Agreement no. 341225. All authors gratefully acknowledge the Van Gogh Program 2016 under no. 35530VM. Finally, the authors are thankful for the valuable comments by three anonymous referees, who have contributed to improving the manuscript.

Appendix A. An equation for the swelling rate of an individual particle

The swelling of a particle is governed by the diffusion of water molecules into the particle. Consider a spherical particle with initial radius r_i^0 and radius $r_i(t)$ at later times. We introduce a local concentration of water $c_i^w(r, t)$ within the SAP grain, which is defined as the mass of water per unit volume. Similarly, $c_i^s(r, t)$ is the local solid mass concentration. Local volume fractions θ_w and θ_s are also defined as the volume of water and solid, respectively, per unit volume of space, such that:

$$\theta_w + \theta_s = 1 \quad (\text{A1})$$

If the mass density of pure water and solid are denoted by ρ_w and ρ_s , respectively, Eq. (A1) can be recast in the following form:

$$\frac{c_i^w}{\rho_w} + \frac{c_i^s}{\rho_s} = 1 \quad (\text{A2})$$

The particle has a volume $V_i(t)$, water mass $M_i^w(t) = \int_0^{r_i} 4\pi r^2 c_i^w(r, t) dr$, and solid mass $M_i^s = \int_0^{r_i} 4\pi r^2 c_i^s(r, t) dr$, which is a constant. They are related by:

$$V_i = V_i^w + V_i^s = \frac{M_i^w}{\rho_w} + \frac{M_i^s}{\rho_s} \quad (\text{A3})$$

Assuming radially symmetric diffusion of water into the particle, the local mass balance equation reads:

$$\frac{\partial c_i^w}{\partial t} = \frac{D}{r^2} \frac{\partial}{\partial r} \left(r^2 \frac{\partial c_i^w}{\partial r} \right), 0 \leq r \leq r_i \quad (\text{A4})$$

where D [$\text{L}^2 \text{T}^{-1}$], the diffusion coefficient of water into the particle, is assumed to be constant. The initial condition is $c_i^w(0) = 0$, and boundary conditions are:

$$\begin{cases} \frac{\partial c_i^w}{\partial t} = 0 & \text{at } r = 0 \\ c_i^w = c_i^w|_{r_i} & \text{at } r = r_i \end{cases} \quad (\text{A5})$$

The second boundary condition is based on the assumption of local equilibrium at the grain surface. We multiply Eq. (A4) by $4\pi r^2$ and subsequently integrate over r :

$$\int_0^{r_i} \frac{\partial c_i^w}{\partial t} 4\pi r^2 dr = \int_0^{r_i} \frac{D}{r^2} \frac{\partial}{\partial r} \left(r^2 \frac{\partial c_i^w}{\partial r} \right) 4\pi r^2 dr \quad (A6)$$

We apply Leibniz integral rule to the left-hand side of Eq. (A6) and integrate the right-hand side and use boundary conditions A5. We obtain:

$$\frac{d}{dt} \left\{ \int_0^{r_i} 4\pi r^2 c_i^w(r, t) dr \right\} - 4\pi r_i^2 c_i^w|_{r_i} \frac{dr_i}{dt} = 4\pi r_i^2 D \frac{\partial c_i^w}{\partial r} \Big|_{r_i} \quad (A7)$$

The term inside the curly bracket is equal to the total mass of water in the grain, $M_i^w(t)$. The term $4\pi r_i^2 \frac{dr_i}{dt}$ can be replaced by $\frac{4\pi}{3} \frac{dr_i^3}{dt} = \frac{dV_i}{dt}$, which using Eq. (A3) can be written as $\frac{1}{\rho_w} \frac{dM_i^w}{dt}$. Therefore, (A7) is recast in the following form:

$$\left(1 - \frac{c_i^w|_{r_i}}{\rho_w} \right) \frac{dM_i^w}{dt} = 4\pi r_i^2 D \frac{\partial c_i^w}{\partial r} \Big|_{r_i} \quad (A8)$$

We rewrite the term in brackets on the left-hand side of Eq. (A8) as $\frac{c_i^s|_{r_i}}{\rho_s}$, following Eq. (A2). Then, we assume that on the surface of the particle, the maximum water concentration is reached such that $\frac{c_i^s|_{r_i}}{\rho_s} = \frac{M_i^s}{\rho_s V_i^{max}} = \frac{4\pi}{3V_i^{max}} (r_i^0)^3$, with V_i^{max} being the maximum volume of the particle. Then, Eq. (A8) becomes:

$$\frac{4\pi (r_i^0)^3}{3V_i^{max}} \frac{dM_i^w}{dt} = 4\pi r_i^2 D \frac{\partial c_i^w}{\partial r} \Big|_{r_i} \quad (A9)$$

We approximate $\frac{\partial c_i^w}{\partial r} \Big|_{r_i}$ by $\frac{c_i^w|_{r_i} - \bar{c}_i^w}{\alpha r_i}$ where αr_i is the distance from r_i to a location in the SAP particle at which c_i^w is equal to the average water concentration $\bar{c}_i^w(t)$. Finally, we note that $\frac{M_i^s}{\rho_s} = \frac{4\pi}{3} (r_i^0)^3$. With these considerations, Eq. (A9) becomes:

$$\frac{1}{V_i^{max}} \frac{dM_i^w}{dt} = \frac{3D}{\alpha} \frac{r_i}{(r_i^0)^3} \left(\frac{M_i^s (Q^{max} - 1)}{V_i^{max}} - \frac{M_i^w}{V_i} \right) \quad (A10)$$

Eq. (A10) is multiplied by V_i^{max} and divided by M_i^s , and the definition of Q_i^{abs} is used such that we obtain:

$$\frac{dQ_i^{abs}}{dt} = \frac{3D}{\alpha} \frac{r_i}{(r_i^0)^3} \left(Q^{max} - 1 - \frac{M_i^w V_i^{max}}{M_i^s V_i} \right) \quad (A11)$$

We can show that $\frac{V_i^{max}}{V_i}$ is approximated by $\frac{Q^{max}}{Q_i^{abs}}$, such that Eq. (A10) is reduced to:

$$\frac{dQ_i^{abs}}{dt} = K_i \left(\frac{Q^{max} - Q_i^{abs}}{Q_i^{abs}} \right) \quad (A12)$$

$$K_i = \frac{3D}{\alpha} \frac{r_i}{(r_i^0)^3}$$

Eq. (A12) bears similarities with an equation reported previously in the literature, namely: $\frac{dQ_i^{abs}}{dt} = K_i (Q^{max} - Q_i^{abs})$, which is a first-order

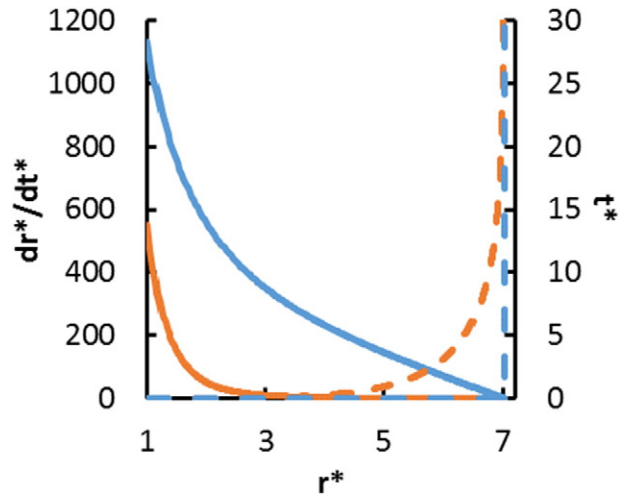


Fig. 11. Swelling rates for the swelling of individual particles, using dimensionless parameters: $t^* = \frac{-D}{(r_i^0)^2}$ and $r^* = \frac{r_i}{r_i^0}$. Solid lines indicate $\frac{dr_i}{dt}$ and dashed lines indicates t^* . Orange represents results by Eq. (A12) whereas blue represents results with $\frac{dQ_i^{abs}}{dt} = \frac{\pi^2 D}{(r_i^0)^2} (Q^{max} - Q_i^{abs})$. (For interpretation of the references to colour in this figure legend, the reader is referred to the web version of this article.)

kinetic rate for the increase of Q_i^{abs} [11,13]. In Eq. (A12), $K_i \propto \frac{r_i}{(r_i^0)^3}$, which reduces to $K_i \propto \frac{1}{(r_i^0)^2}$ for small-scale swelling, which is indeed reported in the literature as $K_i = \frac{\pi^2 D}{(r_i^0)^2}$ [11,13]. We have calculated the difference between Eq. (A12) and $\frac{dQ_i^{abs}}{dt} = K_i (Q^{max} - Q_i^{abs})$ with $K_i = \frac{\pi^2 D}{(r_i^0)^2}$ as reported in [11], which is shown in Fig. 11. That Figure shows that the swelling rate $\frac{dr_i}{dt}$ for both definitions of K_i exhibits the same monotonic decrease of $\frac{dr_i}{dt}$ with r_i , albeit that they differ from each other.

References

- [1] H.G. Diersch, V. Clausnitzer, V. Myrmy, R. Rosati, M. Schmidt, H. Beruda, ... R. Virgilio, Modeling unsaturated flow in absorbent swelling porous media: part 1. Theory, *Transp. Porous Media* 83 (3) (2010) 437–464.
- [2] H.G. Diersch, V. Clausnitzer, V. Myrmy, R. Rosati, M. Schmidt, H. Beruda, ... R. Virgilio, Modeling unsaturated flow in absorbent swelling porous media: part 2. Numerical simulation, *Transp. Porous Media* 86 (3) (2011) 753–776.
- [3] E. Romero, G. Della Vecchia, C. Jommi, An insight into the water retention properties of compacted clayey soils, *Géotechnique* 61 (4) (2011) 313–328.
- [4] P.S. Takhar, Unsaturated fluid transport in swelling poroviscoelastic biopolymers, *Chem. Eng. Sci.* 109 (2014) 98–110.
- [5] M.A. Murad, J.H. Cushman, Multiscale flow and deformation in hydrophilic swelling porous media, *Int. J. Eng. Sci.* 34 (3) (1996) 313–338.
- [6] J.M. Huyghe, J. Janssen, Quadriphasic mechanics of swelling incompressible porous media, *Int. J. Eng. Sci.* 35 (8) (1997) 793–802.
- [7] K. Malakpoor, E.F. Kaasschieter, J.M. Huyghe, Mathematical modelling and numerical solution of swelling of cartilaginous tissues. Part I: modelling of incompressible charged porous media, *ESAIM Math. Model. Numer. Anal.* 41 (04) (2007) 661–678.
- [8] K. Kabiri, H. Omidian, S. Hashemi, M. Zohuriaan-Mehr, Synthesis of fast-swelling superabsorbent hydrogels: effect of crosslinker type and concentration on porosity and absorption rate, *Eur. Polym. J.* 39 (7) (2003) 1341–1348.
- [9] Brandt, Kerry A., Stephen A. Goldman, and Thomas A. Inglin. "Hydrogel-forming polymer compositions for use in absorbent structures." U.S. Patent No. 4,654,039. 31 Mar. 1987.
- [10] A. Knaebel, S. Rebre, F. Lequeux, Determination of the elastic modulus of superabsorbent gel beads, *Polym. Gels Netw.* 5 (2) (1997) 107–121.
- [11] F.L. Buchholz, A.T. Graham, *Modern Superabsorbent Polymer Technology*, John! Wiley & Sons, 1998.

- [12] H. Omidian, S. Hashemi, P. Sammes, I. Meldrum, Modified acrylic-based superabsorbent polymers (dependence on particle size and salinity), *Polymer* 40 (7) (1999) 1753–1761.
- [13] L.P. Esteves, Superabsorbent polymers: on their interaction with water and pore fluid, *Cem. Concr. Compos.* 33 (7) (2011) 717–724.
- [14] A.T. Graham, L.R. Wilson, Commercial processes for the manufacture of superabsorbent polymers, *Modern Superabsorbent Polymer Technology*, Wiley, New York 1998, pp. 69–114.
- [15] Wang, Lin, Ebrahim Rezaei, and Yumiko Hayashi. "Absorbent materials having improved absorbent property and methods for making the same." U.S. Patent No. 5,849,405. 15 Dec. 1998.
- [16] T. Torskaya, V. Shabro, C. Torres-Verdín, R. Salazar-Tio, A. Revil, Grain shape effects on permeability, formation factor, and capillary pressure from pore-scale modeling, *Transp. Porous Media* 102 (1) (2014) 71–90.
- [17] G. Cho, J. Dodds, J.C. Santamarina, Particle shape effects on packing density, stiffness, and strength: natural and crushed sands, *J. Geotech. Geoenviron.* 132 (5) (2006) 591–602.
- [18] K. Terzaghi, R.B. Peck, *Soil Mechanics in Engineering Practice*, 2d ed. J. Wiley, 1968.
- [19] D.R. Chambers, H.H. Fowler Jr., Y. Fujiura, F. Masuda, *Super-Absorbent Polymer Having Improved Absorbency Properties*, 1992.
- [20] Kainth, Arvinder Pal Singh, et al. "Superabsorbent materials having low, controlled gel-bed friction angles and composites made from the same." U.S. Patent No. 7,297,395. 20 Nov. 2007.
- [21] P.A. Cundall, O.D. Strack, A discrete numerical model for granular assemblies, *Geotechnique* 29 (1) (1979) 47–65.
- [22] N. Belheine, J. Plassiard, F. Donzé, F. Darve, A. Seridi, Numerical simulation of drained triaxial test using 3D discrete element modeling, *Comput. Geotech.* 36 (1) (2009) 320–331.
- [23] Ł. Widuliński, J. Kozicki, J. Tejchman, Numerical simulations of triaxial test with sand using DEM, *Arch. Hydro-Eng. Environ. Mech.* 56 (3–4) (2009) 149–172.
- [24] Y. Wang, F. Tonon, Calibration of a discrete element model for intact rock up to its peak strength, *Int. J. Numer. Anal. Methods Geomech.* 34 (5) (2010) 447–469.
- [25] C. Coetzee, D. Els, Calibration of discrete element parameters and the modelling of silo discharge and bucket filling, *Comput. Electron. Agric.* 65 (2) (2009) 198–212.
- [26] J. Plassiard, N. Belheine, F. Donzé, A spherical discrete element model: calibration procedure and incremental response, *Granul. Matter* 11 (5) (2009) 293–306.
- [27] F. Zhang, B. Damjanac, H. Huang, Coupled discrete element modeling of fluid injection into dense granular media, *J. Geophys. Res. Solid Earth* 118 (6) (2013) 2703–2722.
- [28] A.K. Jain, R. Juanes, Preferential mode of gas invasion in sediments: grain-scale mechanistic model of coupled multiphase fluid flow and sediment mechanics, *J. Geophys. Res. Solid Earth* 114 (B8) (2009).
- [29] A. Kharaghani, T. Metzger, E. Tsotsas, A proposal for discrete modeling of mechanical effects during drying, combining pore networks with DEM, *AIChE J.* 57 (4) (2011) 872–885.
- [30] D.F. Boutt, B.K. Cook, B.J. McPherson, J.R. Williams, Direct simulation of fluid-solid mechanics in porous media using the discrete element and lattice-Boltzmann methods, *J. Geophys. Res. Solid Earth* 112 (B10) (2007).
- [31] Y. Tsuji, T. Kawaguchi, T. Tanaka, Discrete particle simulation of two-dimensional fluidized bed, *Powder Technol.* 77 (1) (1993) 79–87.
- [32] B. Chareyre, A. Cortis, E. Catalano, E. Barthélemy, Pore-scale modeling of viscous flow and induced forces in dense sphere packings, *Transp. Porous Media* 94 (2) (2012) 595–615.
- [33] E. Catalano, B. Chareyre, E. Barthélemy, Pore-scale modeling of fluid-particles interaction and emerging poromechanical effects, *Int. J. Numer. Anal. Methods Geomech.* 38 (1) (2014) 51–71.
- [34] E.P. Montellà, M. Toraldo, B. Chareyre, L. Sibille, Localized fluidization in granular materials: theoretical and numerical study, *Phys. Rev. E* 94 (5) (2016), 052905.
- [35] A. Tong, E. Catalano, B. Chareyre, Pore-scale flow simulations: model predictions compared with experiments on bi-dispersed granular assemblies, *Oil Gas Sci. Technol. Rev. Energ. Nouv.* 67 (5) (2012) 743–752.
- [36] V. Šmilauer, E. Catalano, B. Chareyre, S. Dorofeenko, J. Duriez, A. Gladky, ... L. Sibille, Yade reference documentation, Yade Documentation, 2nd ed., 2015, <http://dx.doi.org/10.5281/zenodo.34073>.
- [37] K.L. Johnson, K.L. Johnson, *Contact Mechanics*, Cambridge university Press, 1987.
- [38] C. Thornton, S.J. Cummins, P.W. Cleary, An investigation of the comparative behaviour of alternative contact force models during elastic collisions, *Powder Technol.* 210 (3) (2011) 189–197.
- [39] C. Modenese, S. Utili, G.T. Houlsby, DEM modelling of elastic adhesive particles with application to lunar soil, *Earth Space* 1 (2012) 45–54.
- [40] A.J.H. Frijns, J. Huyghe, J.D. Janssen, A validation of the quadruphase mixture theory for intervertebral disc tissue, *Int. J. Eng. Sci.* 35 (15) (1997) 1419–1429.
- [41] T. Sweijen, E. Nikoee, S.M. Hassanizadeh, B. Chareyre, The effects of swelling and porosity change on capillarity: DEM coupled with a pore-unit assembly method, *Transp. Porous Media* 113 (1) (2016) 207–226.
- [42] V. Mirnyy, V. Clausnitzer, H.G. Diersch, R. Rosati, M. Schmidt, H. Beruda, Wicking in absorbent swelling porous materials, *Tradit. Mod. Model. Approaches Wicking Porous Mater.* (2012) 161–200.
- [43] A. Lorenz, C. Tuozzolo, M.Y. Louge, Measurements of impact properties of small, nearly spherical particles, *Exp. Mech.* 37 (3) (1997) 292–298.
- [44] I. Cavarretta, I. Rocchi, M.R. Coop, A new interparticle friction apparatus for granular materials, *Can. Geotech. J.* 48 (12) (2011) 1829–1840.